INORGANIC CHEMISTRY FRONTIERS

RESEARCH ARTICLE

View Article Online
View Journal

Cite this: DOI: 10.1039/d6qi00521g

An abnormal decrease in Curie temperature in pseudohalide rare-earth double perovskite ferroelastics driven by lanthanide contraction

Meng-Jun Lin, Jun-Ying Li, Pei-Guo Liu, Ya-Ting Zou, Hao-Fei Ni, Lei Pan, Gele Teri, Chang-Feng Wang, * Da-Wei Fu* and Yi Zhang *

Received 18th March 2026,
Accepted 29th April 2026

DOI: 10.1039/d6qi00521g

rsc.li/frontiers-inorganic

Hybrid rare-earth double perovskites (HREDPs) have received increasing attention due to their structural tunability and multifunctionality. However, the impact of lanthanide contraction on the properties of HREDPs remains to be investigated. Herein, we synthesized a series of isostructural HREDP ferroelastics, $(DMSOX)_2LnCs(NO_3)_6$ (DMSOX = dimethylsulfoximine and Ln = La^{3+}, Ce^{3+}, Pr^{3+}, Nd^{3+}, Sm^{3+}, and Eu^{3+}). The results demonstrate that decreasing the rare-earth ionic radius modulates the Curie temperature (T_C), exhibiting a monotonic decrease from 411.1 to 395.8 K across the lanthanide series. Structural analysis reveals that the shrinkage of the ionic radius weakens hydrogen bonding interactions, which is the primary origin of the lowered T_C. Among them, Eu-based $(DMSOX)_2EuCs(NO_3)_6$ possesses an orange-red luminescence behavior with a lifetime of 4.87 ms and a quantum yield of 44%. This work provides a distinct strategy for fine-tuning multifunctional HREDP materials.

Introduction

Perovskite materials have garnered significant research interest due to their exceptional physical properties, including ferroelectricity, piezoelectricity, pyroelectricity, second harmonic generation (SHG), and superconductivity.[1–12] Consequently, perovskite materials have recently experienced rapid development, giving rise to diverse families, such as lead-based halide perovskites, lead-free halide double perovskites, metal-free perovskites, and formate perovskites.[13–26] Among them, as an emerging perovskite family, hybrid rare-earth double perovskites (HREDPs) have demonstrated extraordinary potential, owing to the unique 4f electron configurations and variable coordination geometries of rare-earth cations.[27–33] In 2020, Shi *et al.* reported the first two-dimensional (2D) HREDP, $(R/S\text{-}3HQ)_4KCe(NO_3)_8$ (R/S-3HQ = R/S-hydroxylquinuclidinium), which exhibits room-temperature ferroelectricity and photoluminescence.[30] Subsequently, 3D HREDPs were demonstrated, which possess relaxor ferroelasticity and large piezoelectric responses.[29] Using molecular engineering, Wang *et al.* designed an HREDP ferroelectric with out-of-plane polarization and circularly polarized luminescence (CPL).[34] Our group designed 3D rare-earth double perovskite ferroelectrics with the highest Curie temperature through cation regulation and perovskite framework substitution and explored their application in the field of X-ray detection.[31]

Lanthanide contraction, featuring the progressive decrease in ionic radii across the lanthanide series, has served as a powerful tool for precisely tailoring the physicochemical properties of functional materials.[9,35–40] For instance, Escudero-Escribano *et al.* utilized lanthanide contraction in Pt–lanthanide alloys to tune the surface compressive strain, thereby optimizing the oxygen reduction activity.[41] Li *et al.* demonstrated that substituting smaller lanthanide ions can effectively suppress the disorder of organic cations in polyiodides, optimizing the SHG responses.[42] Despite these advances, the specific effects of lanthanide contraction on the properties of HREDPs have not been fully explored.

In this work, we investigate the influence of lanthanide contraction on the Curie temperature (T_C) of a newly synthesized series of HREDP ferroelastics, $(DMSOX)_2LnCs(NO_3)_6$ (DMSOX = dimethylsulfoximine and Ln = La^{3+}, Ce^{3+}, Pr^{3+}, Nd^{3+}, Sm^{3+}, and Eu^{3+}). Our results demonstrate that the T_C can be modulated by the ionic size of rare-earth elements, exhibiting a decreasing trend as the ionic radius decreases (Scheme 1). Structural analysis reveals that as the ionic radius of the rare-earth ion decreases, the N–H···O hydrogen bond angles between organic cations and inorganic frameworks are progressively reduced, indicating a weakening of hydrogen bonding interactions that leads to a lowering of the phase transition temperature. Furthermore, the Eu-based HREDP

Institute for Science and Applications of Molecular Ferroelectrics, Key Laboratory of the Ministry of Education for Advanced Catalysis Materials, Zhejiang Normal University, Jinhua, 321004, China. E-mail: wang1215@zjnu.edu.cn, dawei@zjnu.edu.cn, yizhang1980@seu.edu.cn

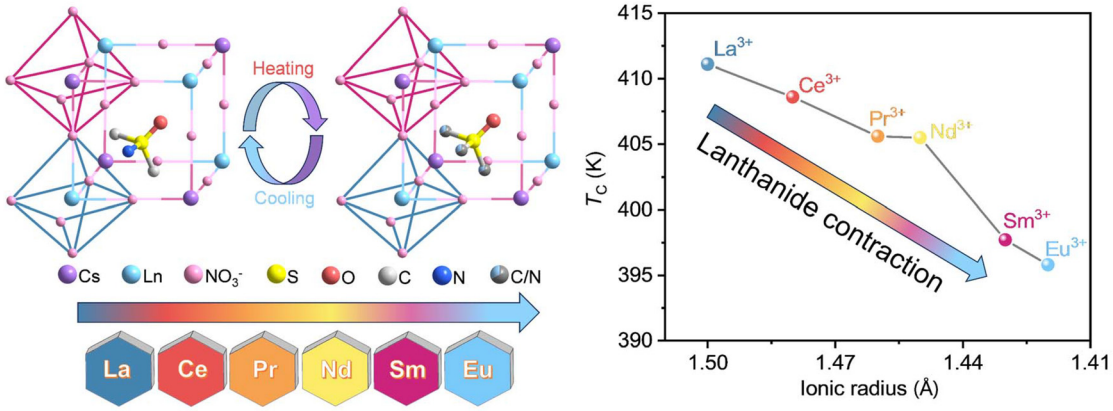

Scheme 1 Lanthanide contraction induces a decrease in T_C in $(DMSOX)_2LnCs(NO_3)_6$.

$(DMSOX)_2EuCs(NO_3)_6$ exhibits typical orange-red luminescence behavior, with a lifetime of 4.87 ms and a quantum yield of 44%.

Results and discussion

Thermal and dielectric properties

$(DMSOX)_2LnCs(NO_3)_6$ single crystals (DMSOX = dimethylsulfoximine and Ln = La^{3+}, Ce^{3+}, Pr^{3+}, Nd^{3+}, Sm^{3+}, and Eu^{3+}) were grown *via* slow evaporation of aqueous solutions containing $(DMSOX)NO_3$, $CsNO_3$, and $Ln(NO_3)_3{\cdot}6H_2O$ in the molar ratio of 2 : 1 : 1 (Fig. S1). Powder X-ray diffraction (PXRD) measurements confirmed their phase purity (Fig. S2). Thermogravimetric analysis (TGA) measurements indicate that the decomposition temperatures of $(DMSOX)_2LnCs(NO_3)_6$ are 480 K (La^{3+}), 478 K (Ce^{3+}), 476 K (Pr^{3+}), 471 K (Nd^{3+}), 462 K (Sm^{3+}), and 453 K (Eu^{3+}) (Fig. 1a), exhibiting a continuous downward trend.[43] To investigate the phase transition behavior of $(DMSOX)_2LnCs(NO_3)_6$, we carried out differential scanning calorimetry (DSC) tests. As shown in Fig. 1b, the endothermic peaks of $(DMSOX)_2LnCs(NO_3)_6$ in the heating run were observed at 411.1 K (La^{3+}), 408.6 K (Ce^{3+}), 405.6 K (Pr^{3+}), 405.5 K (Nd^{3+}), 397.7 K (Sm^{3+}), and 395.8 K (Eu^{3+}), while the corresponding exothermic peaks appeared in the cooling run, confirming the reversible phase transition (Fig. S3). The thermal hysteresis ranges from 6.7 to 11.2 K, and the enthalpy change (ΔH) ranges from 2.640 to 3.062 kJ mol^{-1} (Table S1), which are characteristics indicative of a first-order phase transition. Notably, the phase transition temperature of the $(DMSOX)_2LnCs(NO_3)_6$ decreases as the rare-earth ion radius decreases, exhibiting a trend governed by lanthanide contraction (Fig. 1b). Furthermore, the dielectric constant measurement as a function of temperature corroborated this phenomenon. As shown in Fig. 1c, the real part of the dielectric constant (ε') increases continuously with temperature and presents an anomaly at the phase transition temperature; the corresponding cooling curves also display similar dielectric

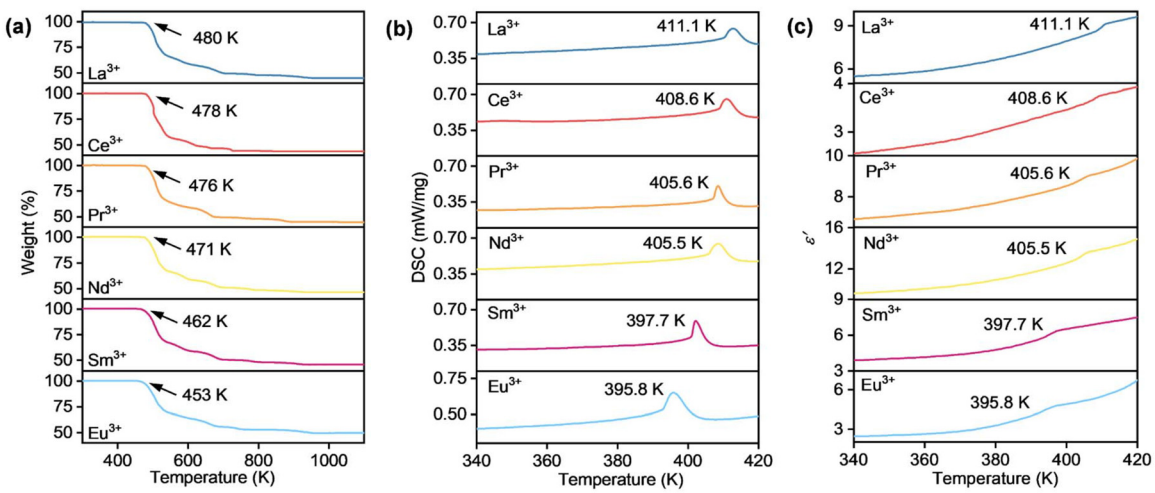

Fig. 1 (a) TGA curves of $(DMSOX)_2LnCs(NO_3)_6$. (b) DSC curve of $(DMSOX)_2LnCs(NO_3)_6$ in the heating run. (c) Temperature-dependent ε' of $(DMSOX)_2LnCs(NO_3)_6$ at 1 MHz.

anomaly behavior (Fig. S4), in agreement with the results of DSC measurements.[44,45]

Crystal structure analysis

To elucidate the phase transition mechanism, crystal structures of $(DMSOX)_2LnCs(NO_3)_6$ (Ln = La^{3+}, Ce^{3+}, Pr^{3+}, Nd^{3+}, Sm^{3+}, and Eu^{3+}) were determined *via* single-crystal X-ray diffraction. For convenience, the phases before and after the transition are referred to as the ferroelastic phase (FP) and paraelastic phase (PP), respectively. Due to their similar crystal structures and phase transition mechanisms, we selected $(DMSOX)_2EuCs(NO_3)_6$ as a representative example for detailed discussion. The structural data for the remaining compounds are shown in the SI (Fig. S5–S9 and Tables S2–S6). As illustrated in Fig. 2a, in the FP, $(DMSOX)_2EuCs(NO_3)_6$ crystallizes in the triclinic space group $P\bar{1}$ with the unit cell parameters: a = 9.120(6) Å, b = 9.139(6) Å, c = 9.147(6) Å, γ = 63.85(2)°, and V = 614.2(7) Å^3 (Table S7). $(DMSOX)_2EuCs(NO_3)_6$ features a typical three-dimensional (3D) double perovskite framework characterized by a corner-sharing network of $Eu(NO_3)_6$ and $Cs(NO_3)_6$ octahedra. Ordered DMSOX organic cations occupy the interstitial cavities, and their oxygen atoms form strong coordination bonds with Cs^+ cations (Fig. 2b).[46] In the PP, $(DMSOX)_2EuCs(NO_3)_6$ transforms into the higher-symmetry space group $R\bar{1}$, with the unit cell parameters: $a = b$ = 10.127 Å, c = 21.379 Å, γ = 120°, and V = 1898.8 Å^3 (Fig. 2d, e and Table S7). Notably, the DMSOX organic cations exhibit a threefold substitution disorder around the C_3 rotation axis (Fig. 2c). Based on the above analysis, it is suggested that the phase transition is driven by an order–disorder transition of the organic cations.

Generally, due to the confinement effect, reducing the void volume increases the phase transition energy barrier, resulting in a higher phase transition temperature.[47–52] However, in the $(DMSOX)_2LnCs(NO_3)_6$ series, an anomalous decrease in the T_C is observed with the lanthanide contraction (Tables S1 and S8).[53] To uncover the microscopic mechanism underlying this anomalous phenomenon, we systematically investigated the interactions between the organic cations and the inorganic framework. As shown in Fig. 3a, as the rare-earth ion varies from La^{3+} to Eu^{3+}, the volume of $Ln(NO_3)_6$ octahedra gradually decreases, which in turn reduces the volume of the lattice cavities enclosing the organic cations. This compression of the cavity volume further strains and distorts the hydrogen bonds formed between the organic cations and NO_3^- (Fig. 3b). Specifically, in $(DMSOX)_2LaCs(NO_3)_6$, the DMSOX organic cations can freely adjust to form nearly straight and strong N–H···O hydrogen bonds with the surrounding NO_3^-, with a bond angle of approximately 161.3°. In sharp contrast, in $(DMSOX)_2EuCs(NO_3)_6$, the reduction of cavity volume forced the N–H···O hydrogen bonds to become distorted, with the bond angle decreasing to 158.8° (Fig. 3c). Accordingly, with the decrease in the rare-earth ionic radius, the N–H···O hydrogen bond angle gradually decreases, indicating that the hydrogen bonding interactions between the organic cations and the inorganic framework gradually weaken.[54,55] Such weakened

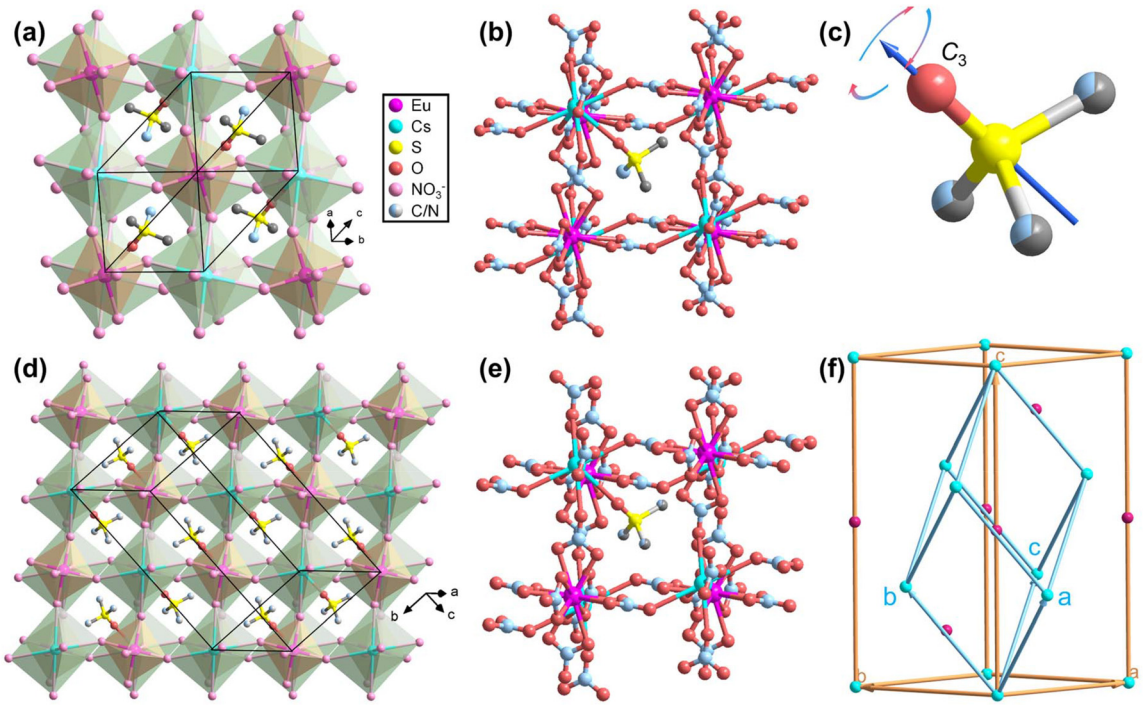

Fig. 2 Packing diagrams of the single crystal structure of $(DMSOX)_2EuCs(NO_3)_6$ in the FP (a) and PP (d). For clarity, the NO_3^- ions were regarded as a ball. The 3D perovskite cage of $(DMSOX)_2EuCs(NO_3)_6$ in the FP (b) and PP (e). (c) Triple substitution disordered DMSOX cation. (f) The relationship of the crystal lattice of $(DMSOX)_2EuCs(NO_3)_6$ between the FP and PP.

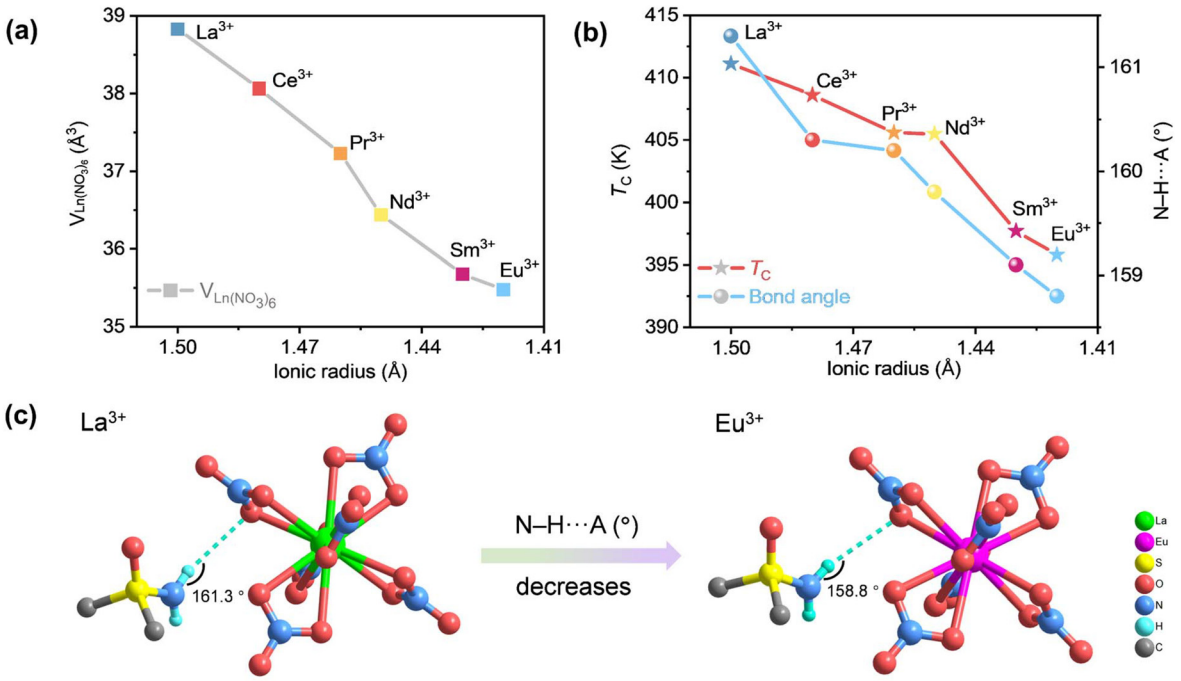

Fig. 3 (a) The relationship between the volume of $Ln(NO_3)_6$ octahedra and the radius of the Ln^{3+} ion. (b) The T_C and N–H···O hydrogen bond angle as a function of the radius of the Ln^{3+} ion. (c) N–H···O hydrogen bond angle in $(DMSOX)_2LaCs(NO_3)_6$ and $(DMSOX)_2EuCs(NO_3)_6$.

interactions reduce the phase transition energy barrier, which ultimately gives rise to the anomalous decrease in the phase transition temperature. Furthermore, we analyzed the origin of the gradual decrease in T_C from a thermodynamic perspective. As the rare-earth ionic radius decreases, ΔH and ΔS exhibit a systematic decreasing trend, consistent with the weakening of hydrogen bonding interactions induced by lanthanide contraction. The systematic evolution of these thermodynamic parameters provides a thermodynamic basis for the gradual decrease in T_C.

Evolution of ferroelastic domains

The symmetry change of $(DMSOX)_2LnCs(NO_3)_6$ corresponds to a ferroelastic phase transition following the Aizu notation $\bar{3}F\bar{1}$. The temperature-dependent evolution of ferroelastic domains constitutes one of the most direct pieces of evidence for ferroelastic materials. Ferroelastic domains with different orientations exhibit distinct birefringence properties, resulting in alternating bright and dark striped patterns.[56] Accordingly, we observed the evolution of ferroelastic domains *via* polarized light microscopy and selected $(DMSOX)_2EuCs(NO_3)_6$ as a representative example for detailed illustration. As shown in Fig. 4b and c, when $(DMSOX)_2EuCs(NO_3)_6$ crystals transform from FP to PP, the striped ferroelastic domains disappear. As $(DMSOX)_2EuCs(NO_3)_6$ crystals revert to FP, the ferroelastic domains reappear (Fig. 4d). Subsequently, during multiple phase transition cycles, the domain structures exhibited consistent changes (Fig. 4e and f), verifying the reversibility of the ferroelastic phase transition (Video S6). No domain structure

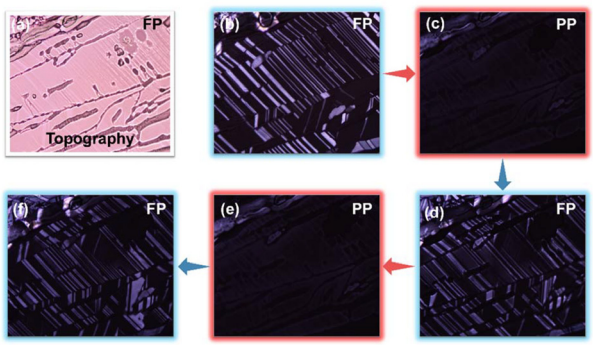

Fig. 4 (a) Topography of the $(DMSOX)_2EuCs(NO_3)_6$ crystal in the FP. (b–f) Evolution of the ferroelastic domain of $(DMSOX)_2EuCs(NO_3)_6$ between the FP and PP.

was detected under natural light (Fig. 4a), proving that the striped patterns are the result of ferroelastic domains rather than the crystal morphology.[57] In addition, the evolution behavior of the ferroelastic domains in $(DMSOX)_2EuCs(NO_3)_6$ under applied stress was investigated. As shown in Fig. S10, after applying stress to the thin film, clear domain wall motion and reorientation were observed. These experimental results confirm the ferroelasticity of $(DMSOX)_2EuCs(NO_3)_6$, demonstrating that the evolution of its ferroelastic domains can be controlled by stress. The evolution of ferroelastic domains of other HREDP ferroelastics is included in the SI (Fig. S11–S15 and Videos S1–S5).

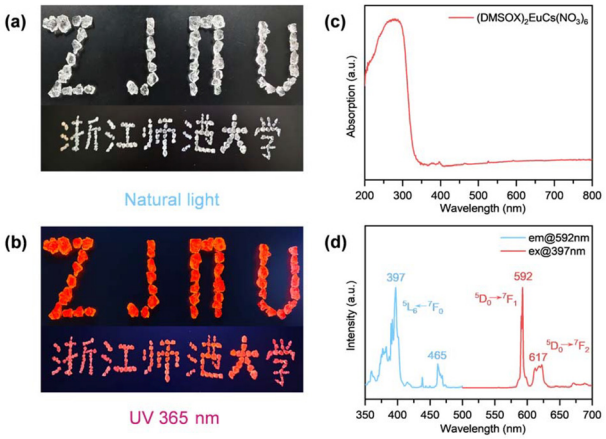

Fig. 5 Optical properties of $(DMSOX)_2EuCs(NO_3)_6$. Photographs of $(DMSOX)_2EuCs(NO_3)_6$ crystals under natural light (a) and 365 nm ultraviolet (UV) irradiation (b). (c) UV-vis absorption spectra of $(DMSOX)_2EuCs(NO_3)_6$. (d) Emission and excitation spectra of $(DMSOX)_2EuCs(NO_3)_6$.

Photoluminescence properties

The incorporation of rare-earth lanthanide ions into hybrid double perovskite frameworks facilitates the achievement of a broad range of fluorescence emission colors.[58] As illustrated in Fig. 5b, under 365 nm ultraviolet (UV) irradiation, $(DMSOX)_2EuCs(NO_3)_6$ crystals (Fig. 5a) exhibit the characteristic orange-red luminescence behavior of Eu^{3+}. Fig. 5d presents the excitation (blue curve) and emission (red curve) spectra of $(DMSOX)_2EuCs(NO_3)_6$. The excitation spectrum features a dominant peak at 396 nm, which matches the absorption spectrum (Fig. 5c) and corresponds to the characteristic $^5L_6 \leftarrow {}^7F_0$ excitation transition of Eu^{3+}. The emission spectrum shows two intense emission peaks: the 592 nm peak arises from the $^5D_0 \rightarrow {}^7F_1$ magnetic dipole transition and the 617 nm peak is attributed to the $^5D_0 \rightarrow {}^7F_2$ electric dipole transition.[31,59] In addition, as shown in Fig. S16, the Commission Internationale de l'Eclairage (CIE) chromaticity coordinates of $(DMSOX)_2EuCs(NO_3)_6$ were (x = 0.6267, y = 0.3732), which is located in the deep orange-red region, consistent with the characteristic red emission originating from the $^5D_0 \rightarrow {}^7F_2$ electric dipole transition of Eu^{3+} ions.[60] Furthermore, the fluorescence lifetime of $(DMSOX)_2EuCs(NO_3)_6$ is 4.87 ms (Fig. S17a), and the photoluminescence quantum yield (QY) reaches 44% (Fig. S17b).

Conclusions

In summary, we synthesized a series of isostructural hybrid rare-earth double perovskite (HREDP) ferroelastics $(DMSOX)_2LnCs(NO_3)_6$ (DMSOX = dimethylsulfoximine and Ln = La^{3+}, Ce^{3+}, Pr^{3+}, Nd^{3+}, Sm^{3+}, and Eu^{3+}) and systematically investigated the impact of lanthanide contraction on their Curie temperature (T_C). Our work demonstrates that continuous shrinkage of the rare-earth ionic radius can modulate the T_C, leading to a monotonic decrease from 411.1 to 395.8 K. The reduction of T_C is attributed to the weakening of hydrogen bonding interactions induced by lanthanide contraction. Our findings offer a precisely controllable strategy for the design and fine-tuning of advanced multifunctional HREDPs.

Author contributions

M.-J. Lin was responsible for the experimental design, execution, and manuscript writing, with a primary focus on the collection and analysis of dielectric and DSC data and the investigation of mechanisms. J.-Y. Li assisted in the observation of ferroelastic domains. P.-G. Liu was responsible for the determination of crystal structures. Y.-T. Zou was responsible for fluorescence data testing. H.-F. Ni and G. Teri assisted in data analysis. L. Pan was responsible for thermogravimetric data measurement. C.-F. Wang, D.-W. Fu and Y. Zhang supervised and guided this work. All authors collectively discussed the results and participated in the revision of the manuscript.

Conflicts of interest

There are no conflicts to declare.

Data availability

The data supporting this article have been included as part of the supplementary information (SI). Supplementary information: synthesis methods, materials and methods, Fig. S1–S17, Tables S1–S14, and Videos S1–S6. See DOI: **https://doi.org/10.1039/d6qi00521g**.

CCDC 2537242 ($(DMSOX)_2EuCs(NO_3)_6$_423 K), 2537243 ($(DMSOX)_2LaCs(NO_3)_6$_423 K), 2537244 ($(DMSOX)_2NdCs(NO_3)_6$_423 K), 2537245 ($(DMSOX)_2SmCs(NO_3)_6$_423 K), 2537246 ($(DMSOX)_2PrCs(NO_3)_6$_423 K), 2537247 ($(DMSOX)_2CeCs(NO_3)_6$_423 K), 2537248 ($(DMSOX)_2SmCs(NO_3)_6$_300 K), 2537249 ($(DMSOX)_2NdCs(NO_3)_6$_300 K), 2537250 ($(DMSOX)_2PrCs(NO_3)_6$_300 K), 2537251 ($(DMSOX)_2PrCs(NO_3)_6$_300 K), 2537252 ($(DMSOX)_2CeCs(NO_3)_6$_300 K) and 2537253 ($(DMSOX)_2EuCs(NO_3)_6$_300 K) contain the supplementary crystallographic data for this paper.[61a–l]

Acknowledgements

This work was financially supported by the Natural Science Foundation of Zhejiang Province (LQN25B010004 and LZ24B010001), the National Natural Science Foundation of China (22505227, 22371258, and 22375182), and the Science and Technology Plan Project of Jinhua (2026-1-010).

References

1 J. F. Scott, Applications of Modern Ferroelectrics, *Science*, 2007, **315**, 954–959.
2 H. S. Choi, S. Li, I.-H. Park, W. H. Liew, Z. Zhu, K. C. Kwon, L. Wang, I.-H. Oh, S. Zheng, C. Su, Q.-H. Xu, K. Yao, F. Pan and K. P. Loh, Tailoring the coercive field in ferroelectric metal-free perovskites by hydrogen bonding, *Nat. Commun.*, 2022, **13**, 794.
3 K. Ding, P.-G. Liu, Y.-L. Xie, M. Q. Li, Z.-L. Li, B. Zhuang, J.-Y. Liu, J.-X. Li, Y. Wang and D.-W. Fu, A novel zero-dimensional germanium-based ferroelectric hybrid material with dual phase transitions, *Inorg. Chem. Front.*, 2025, **12**, 7541–7547.
4 J. Harada, H. Takahashi, R. Notsuka, M. Takehisa, Y. Takahashi, T. Usui and H. Taniguchi, Ferroelectric Ionic Molecular Crystals with Significant Plasticity and a Low Melting Point: High Performance in Hot-Pressed Polycrystalline Plates and Melt-Grown Crystalline Sheets, *Angew. Chem., Int. Ed.*, 2023, **62**, e202215286.
5 J. Harada, M. Takehisa, Y. Kawamura, H. Takahashi and Y. Takahashi, Plastic/Ferroelectric Crystals with Distorted Molecular Arrangement: Ferroelectricity in Bulk Polycrystalline Films through Lattice Reorientation, *Adv. Electron. Mater.*, 2022, **8**, 2101415.
6 Y. Hu, L. You, B. Xu, T. Li, S. A. Morris, Y. Li, Y. Zhang, X. Wang, P. S. Lee, H. J. Fan and J. Wang, Ferroelastic-switching-driven large shear strain and piezoelectricity in a hybrid ferroelectric, *Nat. Mater.*, 2021, **20**, 612–617.
7 M.-L. Ren, W. Luo, Z.-J. Xu, H.-K. Li, L. Liu, C. Shi, N. Wang, H.-Y. Ye and L.-P. Miao, H/OH substitution achieving high-temperature multiferroicity in a Sn(IV)-based hybrid perovskite, *Inorg. Chem. Front.*, 2024, **11**, 7617–7622.
8 P. Wang, X. Li, H. Ye, Q. Guan, Y. Wang, Y. Geng, C. Zhang, H. Li and J. Luo, Durable dielectric switching and photoresponsivity in a Dion–Jacobson hybrid perovskite semiconductor, *Inorg. Chem. Front.*, 2024, **11**, 2436–2441.
9 H. Xiao, L.-Y. Sheng, S. Chen, R.-K. Huang, C.-H. Zeng, Z.-Y. Du, C.-T. He, W.-X. Zhang and X.-M. Chen, Temperature-tunable multiple dielectric switch in hybrid rare-earth perovskites regulated by hierarchical guest dynamics, lanthanide contraction and doping, *Inorg. Chem. Front.*, 2024, **11**, 5336–5344.
10 J. Yao, Z.-J. Feng, J.-Q. Hu, G.-W. Du, Y.-A. Xiong, H.-R. Ji, T.-T. Sha, X. Zhang, Z.-Y. Jing, Q. Pan, H. Hu and Y.-M. You, Steric effect-induced modulation of crystallographic symmetry: implementing ferroelasticity in molecular ferroelectrics, *Inorg. Chem. Front.*, 2025, **12**, 561–568.
11 Z.-X. Zhang, H.-F. Ni, J.-S. Tang, P.-Z. Huang, J.-Q. Luo, F.-W. Zhang, J.-H. Lin, Q.-Q. Jia, G. Teri, C.-F. Wang, D.-W. Fu and Y. Zhang, Metal-Free Perovskite Ferroelectrics with the Most Equivalent Polarization Axes, *J. Am. Chem. Soc.*, 2024, **146**, 27443–27450.
12 J.-C. Qi, Y. Qin, H. Peng, H.-P. Lv, Y.-J. Bai, X. Shen, Z.-T. Xia and W.-Q. Liao, A *Z*/*E* isomeric cation designed organic-inorganic cadmium chloride ferroelectric with broadband white-light emission, *Sci. China: Chem.*, 2024, **67**, 4167–4174.
13 Y. Zhang, E. Parsonnet, A. Fernandez, S. M. Griffin, H. Huyan, C.-K. Lin, T. Lei, J. Jin, E. S. Barnard, A. Raja, P. Behera, X. Pan, R. Ramesh and P. Yang, Ferroelectricity in a semiconducting all-inorganic halide perovskite, *Sci. Adv.*, 2022, **8**, eabj5881.
14 H.-Y. Ye, Y.-Y. Tang, P.-F. Li, W.-Q. Liao, J.-X. Gao, X.-N. Hua, H. Cai, P.-P. Shi, Y.-M. You and R.-G. Xiong, Metal-free three-dimensional perovskite ferroelectrics, *Science*, 2018, **361**, 151–155.
15 A. Ciżman, D. A. Kowalska, P. Szarek, W. Medycki, N. A. Wójcik, M. Gusowski, M. Trzebiatowska, A. Bartosiewicz, L. Filevska, P. Staniorowski and E. Jach, Indications of ferroelectric behaviour near room temperature in the organic–inorganic hybrid Q_2CuBr_4, *Dalton Trans.*, 2025, **54**, 15816–15832.
16 H. A. Evans, L. Mao, R. Seshadri and A. K. Cheetham, Layered Double Perovskites, *Annu. Rev. Mater. Res.*, 2021, **51**, 351–380.
17 K. Li, Z.-G. Li, J. Xu, Y. Qin, W. Li, A. Stroppa, K. T. Butler, C. J. Howard, M. T. Dove, A. K. Cheetham and X.-H. Bu, Origin of Ferroelectricity in Two Prototypical Hybrid Organic-Inorganic Perovskites, *J. Am. Chem. Soc.*, 2022, **144**, 816–823.
18 M. Mączka, J. Kudrawiec, K. Fedoruk-Piskorska, D. Stefańska, A. Gągor, M. Drozd, S. Smółka and A. Sieradzki, Effect of Halide Tuning on the Structural, Dielectric, and Optical Properties of Two-Dimensional 2-Chloroethylammonium Lead Halides, *Inorg. Chem.*, 2025, **64**, 4501–4513.
19 A. Mandal, S. Goswami, S. Das, D. Swain and K. Biswas, New Lead-free Hybrid Layered Double Perovskite Halides: Synthesis, Structural Transition and Ultralow Thermal Conductivity, *Angew. Chem., Int. Ed.*, 2024, **63**, e202406616.
20 C.-F. Wang, H. Li, M.-G. Li, Y. Cui, X. Song, Q.-W. Wang, J.-Y. Jiang, M.-M. Hua, Q. Xu, K. Zhao, H.-Y. Ye and Y. Zhang, Centimeter-Sized Single Crystals of Two-Dimensional Hybrid Iodide Double Perovskite (4,4-Difluoropiperidinium)4AgBiI8 for High-Temperature Ferroelectricity and Efficient X-Ray Detection, *Adv. Funct. Mater.*, 2021, **31**, 2009457.
21 C.-F. Wang, H. Li, C. Ning, L. Wang, Q.-F. Luo, T. Li, H.-F. Ni, Z. An, Z.-X. Zhang, J. Wang, D.-W. Fu, M.-G. Ju, K. Zhao and Y. Zhang, Eco-Friendly Preparation of High-Quality Lead-Free Halide Ferroelectric Solid-Solution Toward High-Performance X-ray Detection, *Angew. Chem., Int. Ed.*, 2026, **65**, e25694.
22 Z.-K. Zhu, T. Zhu, J. Wu, S. You, P. Yu, X. Liu, L. Li, C. Ji and J. Luo, Discovering New Type of Lead-Free Cluster-Based Hybrid Double Perovskite Derivatives with Chiral Optical Activities and Low X-Ray Detection Limit, *Adv. Funct. Mater.*, 2023, **33**, 2214660.
23 Z.-T. Xia, H.-P. Chen, J.-C. Qi, H. Peng, X. Shen, Y.-J. Bai, Z.-Y. Wang, T.-E. Yang and W.-Q. Liao, A high phase transition temperature organic-inorganic Sn(IV)-based metal

halide designed by applying amino positional isomerism to the cation, *Inorg. Chem. Front.*, 2025, **12**, 2825–2832.
24 M. Wang, W. Wang, B. Ma, W. Shen, L. Liu, K. Cao, S. Chen and W. Huang, Lead-Free Perovskite Materials for Solar Cells, *Nano-Micro Lett.*, 2021, **13**, 62.
25 J. Zhang, X. Yang, H. Deng, K. Qiao, U. Farooq, M. Ishaq, F. Yi, H. Liu, J. Tang and H. Song, Low-Dimensional Halide Perovskites and Their Advanced Optoelectronic Applications, *Nano-Micro Lett.*, 2017, **9**, 36.
26 T. Wang, G. Zeng, Y. M. Yang, Z. Yang, T. Wang, H. Li, L. Han, X. Yu, X. Xu and X. Ouyang, Advances in Metal Halide Perovskite Scintillators for X-Ray Detection, *Nano-Micro Lett.*, 2025, **17**, 275.
27 Z. Cui, Z. Hu, W. Zhai, L. Wang, Z. Zhang, H. Zhao, W. Li, L. Miao, H. Ye and C. Shi, Hybrid bimetallic rare-earth perovskite with multichannel bistable fatigue resistance for human-body sensing and wearable electronics, *J. Rare Earths*, 2025, DOI: **10.1016/j.jre.2025.10.015**.
28 Z.-B. Hu, C.-F. Wang, T.-T. Sha, C. Shi, L. Ye, H.-Y. Ye, Y. Song, Y.-M. You and Y. Zhang, An Effective Strategy of Introducing Chirality to Achieve Multifunctionality in Rare-Earth Double Perovskite Ferroelectrics, *Small Methods*, 2022, **6**, 2200421.
29 C. Shi, J.-J. Ma, J.-Y. Jiang, M.-M. Hua, Q. Xu, H. Yu, Y. Zhang and H.-Y. Ye, Large Piezoelectric Response in Hybrid Rare-Earth Double Perovskite Relaxor Ferroelectrics, *J. Am. Chem. Soc.*, 2020, **142**, 9634–9641.
30 C. Shi, L. Ye, Z.-X. Gong, J.-J. Ma, Q.-W. Wang, J.-Y. Jiang, M.-M. Hua, C.-F. Wang, H. Yu, Y. Zhang and H.-Y. Ye, Two-Dimensional Organic-Inorganic Hybrid Rare-Earth Double Perovskite Ferroelectrics, *J. Am. Chem. Soc.*, 2020, **142**, 545–551.
31 C.-F. Wang, Y. Yang, Y. Hu, C. Ma, H.-F. Ni, P.-G. Liu, H.-F. Lu, Z.-X. Zhang, J. Wang, Y. Zhang, D.-W. Fu, K. Zhao and Y. Zhang, Exploring Aqueous Solution-Processed Pseudohalide Rare-Earth Double Perovskite Ferroelectrics toward X-Ray Detection with High Sensitivity, *Angew. Chem., Int. Ed.*, 2024, **63**, e202413726.
32 P. Liu, Y. Xie, M. Li, M. Lin, G. Teri, H. Ni, Q. Jia, C. Wang, D. Fu and Y. Zhang, A 12R hexagonal pseudohalide rare-earth double perovskite ferroelastic: $(TMPA)_2EuRb(NO_3)_6$, *J. Rare Earths*, 2025, DOI: **10.1016/j.jre.2025.09.047**.
33 J. Ma, Q. Xu, L. Ye, Q. Wang, Z. Gong, C. Shi, H. Ye and Y. Zhang, Structural phase transition and dielectric switching in an organic-inorganic hybrid rare-earth double perovskite-type compound: $(DMP)_2LaRb(NO_3)_6$ (DMP = N,N-dimethylpyrrolidinium cation), *J. Rare Earths*, 2022, **40**, 937–941.
34 N. Wang, Z.-J. Xu, H.-F. Ni, W. Luo, H.-K. Li, M.-L. Ren, C. Shi, H.-Y. Ye, X.-B. Fu, Y. Zhang and L.-P. Miao, Molecular Engineering Regulation Achieving Out-of-Plane Polarization in Rare-Earth Hybrid Double Perovskites for Ferroelectrics and Circularly Polarized Luminescence, *Angew. Chem., Int. Ed.*, 2024, **63**, e202409796.
35 K. Bai, P. Sun, M. S. Lassoued, C. Fan, C. Huang, Y. Zheng and W. Chen, Effect of lanthanide contraction on a series of "sulfate-templated" transition-rare-earth metal clusters: Synthesis, structures and magnetic properties, *J. Rare Earths*, 2024, **42**, 2150–2155.
36 C. A. Campos-Roldán, R. Chattot, F. Pailloux, A. Zitolo, J. Rozière, D. J. Jones and S. Cavaliere, Lanthanide contraction effect on the alkaline hydrogen evolution and oxidation reactions activity in platinum-rare earth nanoalloys, *J. Mater. Chem. A*, 2024, **12**, 1253–1258.
37 R. B. Jordan, The Lanthanide Contraction: What is Abnormal and Why?, *Inorg. Chem.*, 2025, **64**, 2207–2216.
38 M. Kumar, L.-Q. Li, J. K. Zaręba, L. Tashi, S. C. Sahoo, M. Nyk, S.-J. Liu and H. N. Sheikh, Lanthanide Contraction in Action: Structural Variations in 13 Lanthanide(III) Thiophene-2,5-dicarboxylate Coordination Polymers (Ln = La-Lu, Except Pm and Tm) Featuring Magnetocaloric Effect, Slow Magnetic Relaxation, and Luminescence-Lifetime-based Thermometry, *Cryst. Growth Des.*, 2020, **20**, 6430–6452.
39 H. Reuter, M. Böltken, M. Horstmann and M. Haase, Structural Evolution in a Series of Isomorphous Rare Earth Compounds as Response of Lanthanide Contraction, *Crystals*, 2023, **13**, 1043.
40 X. Zhang, J. L. Sessler and H.-Y. Gong, Synergic regulation of mechanically interlocked molecules via lanthanide-contraction-based metal modulation and constituent ratios, *Sci. China: Chem.*, 2025, **69**, 300–308.
41 M. Escudero-Escribano, P. Malacrida, M. H. Hansen, U. G. Vej-Hansen, A. Velázquez-Palenzuela, V. Tripkovic, J. Schiøtz, J. Rossmeisl, I. E. L. Stephens and I. Chorkendorff, Tuning the activity of Pt alloy electrocatalysts by means of the lanthanide contraction, *Science*, 2016, **352**, 73–76.
42 Z. Li, Y. Shui, Z. Liang, L. Liu, J. Wan, X. Jiang, Z. Lin and H. Liu, Lanthanide Contraction Eliminates Disorder while Holding Robust Second Harmonic Generation in a Series of Polyiodates, *Chem. Mater.*, 2024, **36**, 10351–10360.
43 B. Wang, J. Hong, Y. Yang, H. Zhao, L. Long and L. Zheng, Achievement of a giant piezoelectric coefficient and piezoelectric voltage coefficient through plastic molecular-based ferroelectric materials, *Matter*, 2022, **5**, 1296–1304.
44 W.-J. Xu, K. Romanyuk, J. M. G. Martinho, Y. Zeng, X.-W. Zhang, A. Ushakov, V. Shur, W.-X. Zhang, X.-M. Chen, A. Kholkin and J. Rocha, Photoresponsive Organic-Inorganic Hybrid Ferroelectric Designed at the Molecular Level, *J. Am. Chem. Soc.*, 2020, **142**, 16990–16998.
45 L.-Y. Zhan, Y. Zhou, N. Li, L.-J. Zhang, X.-J. Xi, Z.-Q. Yao, J.-P. Zhao and X.-H. Bu, A High Working Temperature Multiferroic Induced by Inverse Temperature Symmetry Breaking, *J. Am. Chem. Soc.*, 2024, **146**, 5414–5422.
46 W.-F. Deng, Y.-X. Li, Y.-X. Zhao, J.-S. Hu, Z.-S. Yao and J. Tao, Inversion of Molecular Chirality Associated with Ferroelectric Switching in a High-Temperature Two-Dimensional Perovskite Ferroelectric, *J. Am. Chem. Soc.*, 2023, **145**, 5545–5552.
47 L. Dou, A. B. Wong, Y. Yu, M. Lai, N. Kornienko, S. W. Eaton, A. Fu, C. G. Bischak, J. Ma, T. Ding,

N. S. Ginsberg, L.-W. Wang, A. P. Alivisatos and P. Yang, Atomically thin two-dimensional organic-inorganic hybrid perovskites, *Science*, 2015, **349**, 1518–1521.

48 X.-G. Chen, X.-J. Song, Z.-X. Zhang, H.-Y. Zhang, Q. Pan, J. Yao, Y.-M. You and R.-G. Xiong, Confinement-Driven Ferroelectricity in a Two-Dimensional Hybrid Lead Iodide Perovskite, *J. Am. Chem. Soc.*, 2020, **142**, 10212–10218.

49 Z.-Y. Du, Y.-Z. Sun, S.-L. Chen, B. Huang, Y.-J. Su, T.-T. Xu, W.-X. Zhang and X.-M. Chen, Insight into the molecular dynamics of guest cations confined in deformable azido coordination frameworks, *Chem. Commun.*, 2015, **51**, 15641–15644.

50 Z.-Y. Du, T.-T. Xu, B. Huang, Y.-J. Su, W. Xue, C.-T. He, W.-X. Zhang and X.-M. Chen, Switchable Guest Molecular Dynamics in a Perovskite-Like Coordination Polymer toward Sensitive Thermoresponsive Dielectric Materials, *Angew. Chem., Int. Ed.*, 2015, **54**, 914–918.

51 Y. Peng, J. Bie, X. Liu, L. Li, S. Chen, W. Fa, S. Wang, Z. Sun and J. Luo, Acquiring High-*T*C Layered Metal Halide Ferroelectrics via Cage-Confined Ethylamine Rotators, *Angew. Chem., Int. Ed.*, 2020, **60**, 2839–2843.

52 Z. Wu, S. Li, Y. M. Yousry, W. P. D. Wong, X. Wang, T. Ma, Z. Chen, Y. Shao, W. H. Liew, K. Yao, F. Pan and K. P. Loh, Intercalation-driven ferroelectric-to-ferroelastic conversion in a layered hybrid perovskite crystal, *Nat. Commun.*, 2022, **13**, 3104.

53 Y. Q. Jia, Crystal Radii and Effective Ionic Radii of the Rare Earth Ions, *J. Solid State Chem.*, 1991, **95**, 184–187.

54 E. Arunan, G. R. Desiraju, R. A. Klein, J. Sadlej, S. Scheiner, I. Alkorta, D. C. Clary, R. H. Crabtree, J. J. Dannenberg, P. Hobza, H. G. Kjaergaard, A. C. Legon, B. Mennucci and D. J. Nesbitt, Definition of the hydrogen bond, *Pure Appl. Chem.*, 2011, **83**, 1637–1641.

55 T. Steiner, The Hydrogen Bond in the Solid State, *Angew. Chem., Int. Ed.*, 2002, **41**, 48–76.

56 H.-Y. Zhang, C.-L. Hu, Z.-B. Hu, J.-G. Mao, Y. Song and R.-G. Xiong, Narrow Band Gap Observed in a Molecular Ferroelastic: Ferrocenium Tetrachloroferrate, *J. Am. Chem. Soc.*, 2020, **142**, 3240–3245.

57 H.-F. Zhao, Z.-H. Hu and H. Liang, A Tb^{3+}-Based Hybrid Rare-Earth Double Perovskite with Ferroelastic Switching and Long Photoluminescence Lifetime, *Inorg. Chem.*, 2025, **64**, 25305–25310.

58 Q.-H. Zou, Z.-J. Wang, L.-K. Wu, Y. Feng, L.-L. Jiang, J.-R. Li, H.-Y. Ye and C. Shi, Three-Dimensional Bimetallic Ammonium K-Eu Nitrate with a Rare (6,6)-Connected Ion Topology Exhibiting Structural Phase Transition and Photoluminescence Properties, *Inorg. Chem.*, 2024, **63**, 10817–10822.

59 X. Sun, Y. Li, X. Yin, Z. Wei and H. Cai, Chiral Fluorine Engineering in Amine Molecular Design: Toward High-*T*C Multifunctional Rare-Earth Hybrid Double Perovskites, *Small*, 2025, **21**, 250544.

60 Q.-H. Zou, Z.-J. Wang, L.-K. Wu, Y. Feng, L.-L. Jiang, J.-R. Li, H.-Y. Ye and C. Shi, Three-Dimensional Bimetallic Ammonium K–Eu Nitrate with a Rare (6,6)-Connected Ion Topology Exhibiting Structural Phase Transition And Photoluminescence Properties, *Inorg. Chem.*, 2024, **63**, 10817–10822.

61 (*a*) CCDC 2537242: Experimental Crystal Structure Determination, 2026, DOI: **10.5517/ccdc.csd.cc2r56jp**; (*b*) CCDC 2537243: Experimental Crystal Structure Determination, 2026, DOI: **10.5517/ccdc.csd.cc2r56kq**; (*c*) CCDC 2537244: Experimental Crystal Structure Determination, 2026, DOI: **10.5517/ccdc.csd.cc2r56lr**; (*d*) CCDC 2537245: Experimental Crystal Structure Determination, 2026, DOI: **10.5517/ccdc.csd.cc2r56ms**; (*e*) CCDC 2537246: Experimental Crystal Structure Determination, 2026, DOI: **10.5517/ccdc.csd.cc2r56nt**; (*f*) CCDC 2537247: Experimental Crystal Structure Determination, 2026, DOI: **10.5517/ccdc.csd.cc2r56pv**; (*g*) CCDC 2537248: Experimental Crystal Structure Determination, 2026, DOI: **10.5517/ccdc.csd.cc2r56qw**; (*h*) CCDC 2537249: Experimental Crystal Structure Determination, 2026, DOI: **10.5517/ccdc.csd.cc2r56rx**; (*i*) CCDC 2537250: Experimental Crystal Structure Determination, 2026, DOI: **10.5517/ccdc.csd.cc2r56sy**; (*j*) CCDC 2537251: Experimental Crystal Structure Determination, 2026, DOI: **10.5517/ccdc.csd.cc2r56tz**; (*k*) CCDC 2537252: Experimental Crystal Structure Determination, 2026, DOI: **10.5517/ccdc.csd.cc2r56v0**; (*l*) CCDC 2537253: Experimental Crystal Structure Determination, 2026, DOI: **10.5517/ccdc.csd.cc2r56w1**.

